

Investigation of high-spin states in ^{53}Fe

R. du Rietz,¹ S. J. Williams,^{2,*} D. Rudolph,¹ J. Ekman,¹ C. Fahlander,¹ C. Andreoiu,^{1,†} M. Axiotis,³ M. A. Bentley,² M. P. Carpenter,⁴ C. Chandler,² R. J. Charity,⁵ R. M. Clark,⁶ M. Cromaz,⁶ A. Dewald,⁷ G. de Angelis,³ F. Della Vedova,⁸ P. Fallon,⁶ A. Gadea,³ G. Hammond,² E. Ideguchi,^{5,‡} S. M. Lenzi,⁸ A. O. Macchiavelli,⁶ N. Mărginean,³ M. N. Mineva,¹ O. Möller,⁷ D. R. Napoli,³ M. Nespolo,³ W. Reviol,⁵ C. Rusu,³ B. Saha,⁷ D. G. Sarantites,⁵ D. Seweryniak,⁴ D. Tonev,³ and C. A. Ur³

¹*Department of Physics, Lund University, S-22100 Lund, Sweden*

²*School of Chemistry and Physics, Keele University, Keele, Staffordshire ST5 5BG, United Kingdom*

³*Instituto Nazionale di Fisica Nucleare, Laboratori Nazionali di Legnaro, I-35020 Legnaro, Italy*

⁴*Physics Division, Argonne National Laboratory, Argonne, Illinois 60439, USA*

⁵*Chemistry Department, Washington University, St. Louis, Missouri 63130, USA*

⁶*Nuclear Science Division, Lawrence Berkeley National Laboratory, Berkeley, California 94720, USA*

⁷*Institut für Kernphysik der Universität zu Köln, D-50937 Köln, Germany*

⁸*Dipartimento di Fisica dell'Università and INFN, Sezione di Padova, I-35141 Padova, Italy*

(Received 15 April 2005; published 19 July 2005)

The fusion-evaporation reactions $^{28}\text{Si}(^{32}\text{S},1\alpha2p1n)^{53}\text{Fe}$ at 125 MeV and $^{24}\text{Mg}(^{32}\text{S},2p1n)^{53}\text{Fe}$ at a 95-MeV beam energy were used to investigate excited states in ^{53}Fe . The combination of the Gammasphere Ge detector array and ancillary devices led to the construction of an extensive level scheme comprising some 90 transitions connecting 40 states. The lifetime of the yrast $25/2^-$ state and upper limits for the lifetimes of a number of additional states were determined using the Cologne plunger device coupled to the GASP γ -ray spectrometer. The experimental results are compared to large-scale shell-model calculations using different sets of two-body matrix elements. In particular, predictions on electromagnetic decay properties such as lifetimes, branching ratios, and mixing ratios are studied in detail.

DOI: [10.1103/PhysRevC.72.014307](https://doi.org/10.1103/PhysRevC.72.014307)

PACS number(s): 21.60.Cs, 23.20.En, 23.20.Lv, 27.40.+z

I. INTRODUCTION

Nuclei in the vicinity of the doubly magic $N = Z$ nucleus ^{56}Ni as well as $N \sim Z$ nuclei near the middle of the $1f_{7/2}$ shell are well described by large-scale shell-model calculations within the full fp model space [1]. These nuclei offer the possibility for detailed investigations of a large variety of phenomena through the comparison between comprehensive and concise experimental data and theoretical predictions. Examples range from “complete” spectroscopy via the subject of band termination to the possible influence of isospin $T = 0$ or $T = 1$ neutron-proton pairing and isospin symmetry studies in pairs of $T_z = \pm 1/2$ or $T_z = \pm 1$ mirror nuclei.

The latter investigations are always based on a comparison of excitation energies of analog states in so-called mirror energy difference diagrams, which require well-established level schemes of both mirror partners. Such an investigation has recently been presented for the yrast structures in the $A = 53$ mirror pair [2]. Although the experimental information on the neutron-deficient partner often is limited to excitation energies and spins and parities of the excited states, detailed spectroscopy, including electromagnetic decay properties, can be derived—and thus probed—in the less exotic member

of the mirror pair. In turn, these more detailed tests of the interactions and Coulomb effects included in the large-scale shell-model calculations may help to obtain a better understanding of the origin and importance of certain isospin breaking contributions.

This work presents a largely extended level scheme for the ^{53}Fe nucleus, including lifetimes of a few excited states. Previously known low-lying excited states in ^{53}Fe [3] are either adopted or confirmed in the final level scheme. A preliminary analysis of the present data set is described in Refs. [4,5], which includes also additional information from the experiment described in Ref. [2]. The experimental results are compared to large-scale shell-model calculations using two different interactions common for the fp model space. In these calculations the effective charges in the mass $A \sim 50$ –60 region derived in Ref. [6] are employed, and an investigation of effective g factors is performed. In particular, the agreement between experimental and calculated electromagnetic properties such as lifetimes, branching ratios, and mixing ratios is studied.

II. EXPERIMENTS

The present work is based on data from three experiments, two of which were performed under nearly identical conditions using the Argonne Tandem-Linac Accelerator System at Argonne National Laboratory and the 88-Inch Cyclotron at Lawrence Berkeley National Laboratory. These two experiments employed the $^{28}\text{Si}(^{32}\text{S},1\alpha2p1n)^{53}\text{Fe}$ fusion-evaporation

*Present address: School of Chemistry and Physics, University of Surrey, Guildford, Surrey GU2 7XH, UK.

†Present address: Department of Physics, University of Guelph, Guelph, Ontario, N1G 2W1 Canada.

‡Present address: RIKEN, Saitama 351-0198, Japan.

reaction at an effective beam energy on target of 125 MeV. The ^{28}Si targets were enriched to 99.90% and had a thickness of 0.5 mg/cm^2 . They were supported with a 1 mg/cm^2 Au and Ta foil, respectively, which was directed toward the beam. The γ rays were detected in the Gammasphere array [7], which comprised 78 Ge detectors. The Heavimet collimators were removed to allow for γ -ray multiplicity and sum-energy measurements [8]. For the detection of light-charged particles the 4π CsI-array Microball [9] was used, and evaporated neutrons were measured in the Neutron Shell [10], which consists of 30 liquid-scintillator detectors replacing the 30 most forward Ge detectors of Gammasphere. Events with four or more Ge detectors in coincidence or more than three Ge detectors and one neutron in coincidence were written to magnetic tape. At the end of the experiments data were taken with ^{56}Co , ^{133}Ba , and ^{152}Eu standard sources to calibrate the Ge detectors.

The third experiment was conducted at Legnaro National Laboratory, Italy, using the $^{24}\text{Mg}(^{32}\text{S},2p1n)^{53}\text{Fe}$ fusion-evaporation reaction with a beam energy of 95 MeV. The experiment utilized in total three 99.92% isotopically enriched and on average 0.95 mg/cm^2 thick ^{24}Mg targets. Each target was mounted inside the Cologne plunger device [11] in front of a stretched 13 mg/cm^2 gold stopper foil. Data were taken at 21 target-stopper distances ranging from electric contact to 4.0 mm. The γ rays were detected with the GASP detector array [12] using its 40 HPGe detectors (distributed in seven rings at $r_0 = 34.6^\circ$, $r_1 = 59.4^\circ$, $r_2 = 72.0^\circ$, $r_3 = 90.0^\circ$, $r_4 = 108.0^\circ$, $r_5 = 120.6^\circ$, and $r_6 = 145.4^\circ$) and 74 BGO elements. Events with at least one BGO element and two HPGe detectors firing in coincidence were accepted by the event trigger. At the end of the experiment ^{56}Co , ^{133}Ba , and ^{152}Eu standard sources were used to calibrate the detector system.

III. DATA ANALYSIS

A. The Gammasphere experiments

The details of the data analysis of the two Gammasphere experiments have been described earlier [4,13–15]. In short, clean particle gated γ -ray spectra are obtained by employing pulse-shape discrimination techniques to distinguish between protons and α particles detected in Microball and to discriminate between neutrons and γ rays detected in the Neutron Shell. The detection efficiencies for the evaporated particles amount to some 65% for protons, 50% for α particles, and 25% for neutrons. In addition, an event-by-event kinematic reconstruction method was applied to reduce the effect of the Doppler broadening caused by the evaporated particles.

The $1\alpha 2p1n$ reaction channel leads to ^{53}Fe . In the course of the analysis E_γ projections and E_γ - E_γ matrices in coincidence with one α particle, two protons, and one neutron were studied by means of the Radware software package and the spectrum-analysis code TV [16,17] to construct the level scheme and derive the relative intensities of the transitions. Weak contaminations in the $1\alpha 2p1n$ -gated spectra arose from the $1\alpha 3p1n$ channel ^{52}Mn (i.e., when a proton escaped detection) from the $3p1n$ and $4p1n$ channels ^{56}Co and ^{55}Fe

(i.e., when one or two protons were misidentified as an α particle) and from ^{54}Fe , which represents the $1\alpha 2p1n$ channel for reactions on small ^{29}Si target impurities. These contaminants can be suppressed considerably by applying the total energy plane selection method [18] and by eventually subtracting corresponding spectra in coincidence with, for example, one α particle, three protons, and one neutron.

Multipolarity assignments of γ -ray transitions were based on two methods, and we refer to Refs. [13,15,19] for further details. The first method is based on efficiency-corrected intensity ratios, R_{150-97} , of γ -ray transitions detected in the three most backward oriented Ge-detector rings of Gammasphere and Ge detectors placed in the central section of Gammasphere. The ratios were evaluated from γ -ray spectra in coincidence with proper subsets of intense transitions known to belong to ^{53}Fe . These transitions were detected at an average angle of $\bar{\theta} = 124^\circ$, where the relative intensities from different multiplicities are roughly the same. Stretched $E2$ transitions are predicted to have $R_{150-97} \approx 1.2$, whereas stretched $\Delta I = 1$ transitions should have $R_{150-97} \approx 0.8$. $\Delta I = 0$ transitions have values similar to $E2$ transitions, and, of course, all these estimates depend somewhat on the spin alignment of the respective nuclear state.

Directional correlations of oriented states (DCO ratios) defined as follows:

$$R_{\text{DCO}}(150 - 97) = \frac{I(\gamma_1 \text{ at } 150^\circ; \text{ gated with } \gamma_2 \text{ at } 97^\circ)}{I(\gamma_1 \text{ at } 97^\circ; \text{ gated with } \gamma_2 \text{ at } 150^\circ)}$$

were deduced as well. If possible, known stretched $E2$ transitions were used for gating. In this case one expects $R_{\text{DCO}} = 1.0$ for observed stretched $E2$ transitions and ≈ 0.6 for stretched $\Delta I = 1$ transitions. Again, nonstretched $\Delta I = 0$ transitions have values similar to $E2$ transitions. If, however, stretched $M1$ transitions were used for gating, $R_{\text{DCO}} = 1.0$ and ≈ 1.6 is expected for observed stretched $\Delta I = 1$ and $E2$ transitions, respectively.

Deviations from these estimates for $\Delta I = 1$ transitions indicate a nonzero mixing ratio of the respective transition, namely $\delta(E2/M1) > 0$ (< 0) for numbers smaller (larger) than expected for R_{150-97} and $R_{\text{DCO}}(150 - 97)$, respectively. The sign convention of Rose and Brink is applied [20]. Finally, even though stretched $E2$ and $\Delta I = 0$ transitions provide similar angular distribution and correlation ratios, a distinction is usually straightforward because of yrast arguments—in fusion-evaporation reactions the most intense transitions denote the yrast line—and the combination of the numbers of several feeding, decaying, or parallel transitions. A few examples are going to be mentioned in the following section.

B. The GASP experiment

The lifetimes of the yrast $21/2^-$ and $25/2^-$ states in ^{53}Fe are derived by means of the recoil distance Doppler shift (RDDS) technique. The intensities of the unshifted components of the 963 keV $25/2^- \rightarrow 21/2^-$ and the 3325 keV $21/2^- \rightarrow 19/2^-$ transitions are determined in coincidence with the

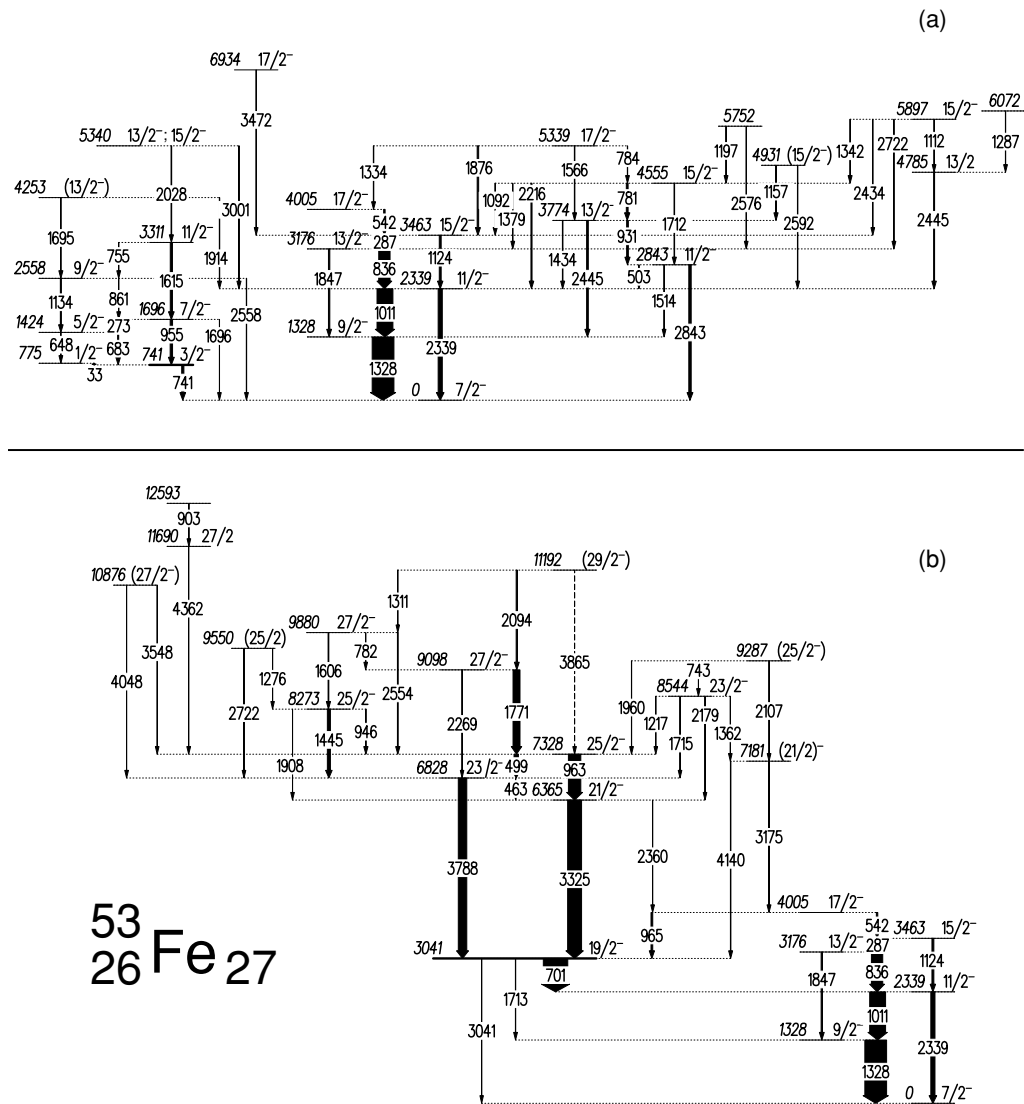


FIG. 1. The proposed level scheme of ^{53}Fe . The top panel (a) provides the “low-spin” regime, which was in part known from previous studies [3], whereas the bottom panel (b) focuses on the “high-spin” part, which is built on the 3041-keV $19/2^-$ spin gap isomer. Energy labels are in kilo-electron-volts. The thickness of the arrows corresponds to the relative intensities of the transitions. Tentative transitions are dashed.

shifted component of the 1771 keV $27/2^- \rightarrow 25/2^-$ transition [cf. Fig. 1(b)]. The RDDS analysis requires shifted and unshifted components of the transitions to be well separated. Therefore, only the two most forward (r_0, r_1) and the two most backward (r_5, r_6) detector rings of GASP are used. For each distance the events were sorted offline into $\gamma\gamma$ coincidence matrices with γ rays detected in one of the given detector rings placed along the axis. In total, 16 matrices ($\gamma_{r_0}\gamma_{r_0}, \gamma_{r_0}\gamma_{r_1}, \dots, \gamma_{r_6}\gamma_{r_5}$, and $\gamma_{r_6}\gamma_{r_6}$) per distance were created.

At first, the position of the shifted components of the 1771-keV transition in rings $\gamma_{r_0}, \gamma_{r_1}, \gamma_{r_5}$, and γ_{r_6} is determined in respective γ -ray spectra in coincidence with the 3325-keV transition. In turn, this information is used for producing for each distance 16 spectra in coincidence with the shifted component of the 1771-keV transition. Four times four of these 16 spectra are taken at the same detector ring (i.e., they can be added together). An example are the four γ_{r_0}

spectra from the $\gamma_{r_0}\gamma_{r_0}, \gamma_{r_0}\gamma_{r_1}, \gamma_{r_0}\gamma_{r_5}$, and $\gamma_{r_0}\gamma_{r_6}$ matrices, whereby the 1771-keV coincidence condition is imposed on the $\gamma_{r_0}, \gamma_{r_1}, \gamma_{r_5}$, and γ_{r_6} axes, respectively. The intensities of the unshifted components of the 963-keV and the 3325-keV transitions can now be measured in these four spectra and are subsequently summed together resulting in one number for each transition and each measured target-stopper distance.

The analysis of the same transition for different distances requires a normalization of its intensity because of, for example, different beam currents or measuring times. The normalization coefficients employed in the current analysis have been determined for each target-stopper distance as described in Ref. [6]. The normalization coefficients are also used as weighting factors when different measurements at about the same distance are combined. Also the recoil velocity for the 21 target-distance combinations has been settled in the

TABLE I. The energies of excited states in ^{53}Fe , the transition energies and relative intensities of the γ rays placed in the level scheme, angular distribution ratios, DCO ratios, the spins and parities of the initial and final states of the γ rays, and the lifetimes of excited states determined in the present study.

E_x (keV)	E_γ (keV)	I_{rel} (%)	R_{150-97}	R_{DCO} $150^\circ-97^\circ$	Mult. Ass.	I_i^π (\hbar)	I_f^π (\hbar)	τ (ps)
741.1(1) ^a	741.1(1) ^a	b			<i>E2</i>	$3/2^-$ ^a	$7/2^-$	
775.4(4) ^a	33.3(1) ^a	b			<i>M1</i>	$1/2^-$ ^a	$3/2^-$	
1328.3(4)	1328.4(6)	100(3)	0.56(2)	0.81(7) ^c	<i>E2/M1</i>	$9/2^-$	$7/2^-$	
1423.7(2)	648.3(2)	1.8(2)	1.26(17)		<i>E2</i>	$5/2^-$ ^a	$1/2^-$	
	682.6(2)	5.2(2)	1.08(8)		<i>E2/M1</i>	$5/2^-$	$3/2^-$	
1696.4(2)	272.8(1)	0.9(2)	0.60(7)		<i>E2/M1</i>	$7/2^-$ ^a	$5/2^-$	
	955.3(5)	11(1)	1.13(8)		<i>E2</i>	$7/2^-$	$3/2^-$	
	1696(1)	0.6(1)			$\Delta I = 0$	$7/2^-$	$7/2^-$	
2339.4(3)	1010.5(5)	72(2)	0.62(3)	0.86(8) ^c	<i>E2/M1</i>	$11/2^-$	$9/2^-$	
	2339(1)	15(2)	1.18(7)	1.58(28) ^c	<i>E2</i>	$11/2^-$	$7/2^-$	
2557.9(4)	861.3(4)	1.6(3)	0.75(9)		<i>M1</i>	$9/2^-$	$7/2^-$	
	1134.2(6)	4.8(4)	1.26(17)		<i>E2</i>	$9/2^-$	$5/2^-$	
	2558(1)	1.5(3)			<i>E2/M1</i>	$9/2^-$	$7/2^-$	
2842.6(4)	503.1(4)	1.8(3)			$\Delta I = 0$	$11/2^-$	$11/2^-$	
	1514(1)	1.2(2)	0.69(14)		<i>M1</i>	$11/2^-$	$9/2^-$	
	2843(1)	12(1)	1.22(9)		<i>E2</i>	$11/2^-$	$7/2^-$	
3040.6(3)	701.1(1) ^a	b			<i>E4</i>	$19/2^-$ ^a	$11/2^-$	
	1712.6(3) ^a	b			<i>M5</i>	$19/2^-$	$9/2^-$	
	3040.6(5) ^a	b			<i>E6</i>	$19/2^-$	$7/2^-$	
3175.8(4)	836.4(4)	50(2)	0.66(3)	0.50(9)	<i>E2/M1</i>	$13/2^-$	$11/2^-$	
	1847(1)	6.2(6)	1.32(10)	1.36(31) ^c	<i>E2</i>	$13/2^-$	$9/2^-$	
3311.2(6)	755.2(5)	2.2(5)			<i>E2/M1</i>	$11/2^-$	$9/2^-$	
	1614.9(8)	10(1)	1.13(8)	0.92(14)	<i>E2</i>	$11/2^-$	$7/2^-$	
3463.0(4)	287.1(1)	38(1)	0.74(3)	0.64(12)	<i>M1</i>	$15/2^-$	$13/2^-$	
	1123.6(6)	8.7(8)	1.39(11)		<i>E2</i>	$15/2^-$	$11/2^-$	
3773.8(5)	931.0(5)	7.8(5)	0.57(5)	0.45(10)	<i>E2/M1</i>	$13/2^-$	$11/2^-$	
	1434(1)	2.5(3)	0.68(9)		<i>M1</i>	$13/2^-$	$11/2^-$	
	2445(1)	7.7(9)	1.17(16)		<i>E2</i>	$13/2^-$	$9/2^-$	
4005.2(4)	542.2(2)	6.6(3)	0.70(5)	1.25(27) ^c		$17/2^-$	$15/2^-$	
	965.0(6)	8.0(8)			<i>E2/M1</i>	$17/2^-$	$19/2^-$	
4253.2(8)	1695(1)	2.6(4)	1.29(14)		(<i>E2</i>)	($13/2^-$)	$9/2^-$	
	1914(1)	1.8(4)	0.91(15)		(<i>E2/M1</i>)	($13/2^-$)	$11/2^-$	
4554.8(4)	780.7(4)	8.2(5)	0.76(8)		<i>M1</i>	$15/2^-$	$13/2^-$	
	1091.8(6)	2.9(4)	1.41(15)		$\Delta I = 0$	$15/2^-$	$15/2^-$	
	1244(1) ^d	0.6(2)			<i>E2</i>	$15/2^-$	$11/2^-$	
	1379.1(7)	1.4(2)			<i>E2/M1</i>	$15/2^-$	$13/2^-$	
	1712(1)	2.6(3)			<i>E2</i>	$15/2^-$	$11/2^-$	
	2216(1)	4.9(4)			<i>E2</i>	$15/2^-$	$11/2^-$	
4784.7(8)	2445(1)	4.5(9)	0.82(10)		$\Delta I = 1$	$13/2^-$	$11/2^-$	
4930.9(9)	1157(1)	3.2(5)	0.94(14)		(<i>E2/M1</i>)	($15/2^-$)	$13/2^-$	
	2592(2)	1.9(3)	1.47(21)		(<i>E2</i>)	($15/2^-$)	$11/2^-$	
5339.3(5)	784.4(5)	1.4(4)			<i>M1</i>	$17/2^-$	$15/2^-$	
	1334(1)	1.2(4)			$\Delta I = 0$	$17/2^-$	$17/2^-$	
	1566(1)	2.3(4)			<i>E2</i>	$17/2^-$	$13/2^-$	
	1876(1)	6.8(3)	0.66(5)	0.85(21) ^c	<i>E2/M1</i>	$17/2^-$	$15/2^-$	
5339.6(9)	2028(1)	2.9(5)				$13/2^-; 15/2^-$	$11/2^-$	
	3001(2)	3.0(7)				$13/2^-; 15/2^-$	$11/2^-$	
5751.5(7)	1196.7(6)	1.3(3)					$15/2^-$	
	1746(1) ^d	2.2(4)					$17/2^-$	
	2576(2)	0.8(2)					$13/2^-$	
5896.9(7)	1112(1)	1.0(3)			$\Delta I = 1$	$15/2^-$	$13/2^-$	
	1342.1(7)	2.3(5)			$\Delta I = 0$	$15/2^-$	$15/2^-$	
	1892(1) ^d	1.5(3)			$\Delta I = 1$	$15/2^-$	$17/2^-$	

TABLE I. (Continued.)

E_x (keV)	E_γ (keV)	I_{rel} (%)	R_{150-97}	R_{pco} $150^\circ-97^\circ$	Mult. Ass.	I_i^π (\hbar)	I_f^π (\hbar)	τ (ps)
	2434(2)	1.0(2)	1.14(21)		$\Delta I = 0$	$15/2^-$	$15/2^-$	
	2722(2)	1.6(2)	0.33(8)		$E2/M1$	$15/2^-$	$13/2^-$	
6071.8(11)	1287.1(7)	1.3(2)					$13/2^-$	
6365.1(11)	2360(2)	0.8(2)	1.51(33)		$E2$	$21/2^-$	$17/2^-$	<4
	3325(2)	64(2)	1.70(7)	1.33(9)	$E2/M1$	$21/2^-$	$19/2^-$	
6689.0(20)	3226(2) ^d	2.4(5)	0.18(5)		$E2/M1$	$17/2^-$	$15/2^-$	
6828.3(11)	463.2(4)	0.6(1)			$M1$	$23/2^-$	$21/2^-$	
	3788(2)	39(1)	1.36(6)		$E2$	$23/2^-$	$19/2^-$	
6933.8(13)	3472(3)	1.2(3)	0.36(12)		$E2/M1$	$17/2^-$	$15/2^-$	
7139.0(30)	3676(3) ^d	1.8(4)	1.20(24)		($E2$)	($19/2^-$)	$15/2^-$	
7181.0(12)	3175(2)	2.0(4)	1.47(19)		($E2$)	($21/2^-$)	$17/2^-$	
	4140(3)	2.2(2)			($E2/M1$)	($21/2^-$)	$19/2^-$	
7214.0(30)	3751(3) ^d	1.4(3)					$15/2^-$	
7327.5(11)	499.3(2)	20(1)	1.09(5)	0.79(7)	$E2/M1$	$25/2^-$	$23/2^-$	26.2(32)
	962.6(5)	57(2)	1.26(5)		$E2$	$25/2^-$	$21/2^-$	
8273.4(11)	945.8(6)	3.4(3)	1.47(10)	1.12(27)	$\Delta I = 0$	$25/2^-$	$25/2^-$	$<0.2^\circ$
	1445(1)	14(1)	1.01(6)	0.65(9)	$E2/M1$	$25/2^-$	$23/2^-$	
	1908(1)	0.5(2)	1.13(23)		$E2$	$25/2^-$	$21/2^-$	
8543.8(11)	1217(1)	0.5(2)	0.51(11)		$E2/M1$	$23/2^-$	$25/2^-$	
	1362(1)	0.6(3)			($E2/M1$)	$23/2^-$	($21/2^-$)	
	1715(1)	0.6(2)	1.27(37)		$\Delta I = 0$	$23/2^-$	$23/2^-$	
	2179(2)	0.6(2)	1.70(39)		$E2/M1$	$23/2^-$	$21/2^-$	
9098.0(13)	1771(1)	32(2)	0.95(4)	0.77(7)	$E2/M1$	$27/2^-$	$25/2^-$	$<0.2^\circ$
	2269(2)	0.3(1)			$E2$	$27/2^-$	$23/2^-$	
9287.4(12)	743(1)	0.6(3)			($M1$)	($25/2^-$)	$23/2^-$	
	1960(1)	1.0(2)	1.14(27)		($\Delta I = 0$)	($25/2^-$)	$25/2^-$	
	2107(1)	1.1(3)			($E2$)	($25/2^-$)	($21/2^-$)	
9549.6(14)	1276(1)	0.4(2)			($\Delta I = 0$)	($25/2^-$)	$25/2^-$	
	2722(2)	0.6(2)	0.72(22)		($\Delta I = 1$)	($25/2^-$)	$23/2^-$	
9880.3(13)	782.3(5)	0.7(2)			$\Delta I = 0$	$27/2^-$	$27/2^-$	$<0.2^\circ$
	1606(1)	3.4(4)	0.99(11)	0.68(19)	$E2/M1$	$27/2^-$	$25/2^-$	
	2554(2)	3.5(3)	1.59(15)		$E2/M1$	$27/2^-$	$25/2^-$	
10875.8(26)	3548(3)	0.6(2)			($E2/M1$)	($27/2^-$)	$25/2^-$	
	4048(4)	0.8(3)	1.17(50)		($E2$)	($27/2^-$)	$23/2^-$	
11191.7(14)	1311(1)	0.4(2)			($E2/M1$)	($29/2^-$)	$27/2^-$	$<0.2^\circ$
	2094(1)	6.0(5)	1.43(10)	1.02(26)	($E2/M1$)	($29/2^-$)	$27/2^-$	
	3865(3)	0.5(2)			($E2$)	($29/2^-$)	$25/2^-$	
11689.5(32)	4362(3)	1.4(2)	0.54(11)		$\Delta I = 1$	$27/2^-$	$25/2^-$	
12592.9(32)	903.4(6)	0.8(2)					$27/2^-$	

^aAdopted from Ref. [3].

^bCannot be determined in the present experiment because of the long lifetime of the initial state.

^cThe pure, stretched 287-keV $15/2^- \rightarrow 13/2^-$ $M1$ transition is used for gating.

^dNot included in the level scheme displayed in Fig. 1.

^eEffective lifetime.

previous analysis. The velocities range from 3.7% to 4.1% of the speed of light for the three different targets used during the experiment. Using these velocities the 21 distances can be converted into 21 flight times, which are combined to 14 effective flight times: 0.339(12), 0.506(12), 0.675(10), 1.09(1), 1.70(2), 2.61(6), 3.99(8), 8.5(9), 14.7(3), 34.8(9), 61.2(14), 105(3), 175(5), and 354(9) ps. Because unshifted components of the 963- and 3325-keV transitions were not visible in the spectra taken at the largest distance, it was excluded from the analysis.

IV. RESULTS

The experimental results are summarized in the deduced excitation scheme of ^{53}Fe shown in Fig. 1 and Table I. For clarity, the deduced level scheme of ^{53}Fe is split in two parts, each of which comprises the $17/2^- \rightarrow 15/2^- \rightarrow 13/2^- \rightarrow 11/2^- \rightarrow 9/2^- \rightarrow 7/2^-$ yrast cascade as a reference. Figure 1(a) shows the levels and transitions directly connected to this yrast cascade, whereas Fig. 1(b) focuses on a high-spin sequence built on the 3041-keV $19/2^-$ isomer

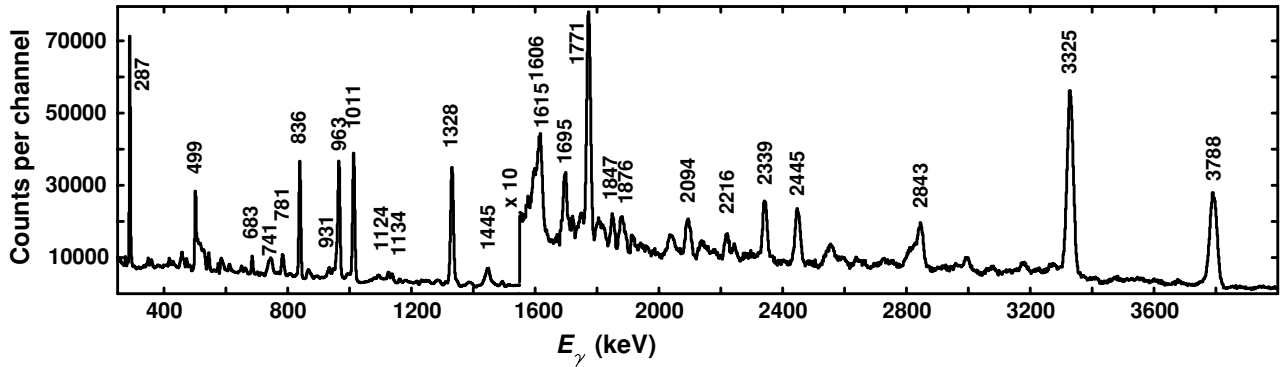


FIG. 2. γ -ray spectrum in coincidence with one α particle, two protons, and one neutron from the two Gammasphere experiments. Small contaminations from ^{52}Mn , $^{54,55}\text{Fe}$, and ^{56}Co were carefully subtracted (see text for details). The most intense transitions are labeled with their energies in kilo-electron-volts.

($T_{1/2} = 2.526(24)$ min [3]). Two weak transitions at 2360 and 3175 keV were found to feed the 4005-keV $17/2^-$ yrast state and thus connect the two parts. Because of the long half-life of the isomer it is impossible to observe the depopulating 701-, 1713-, and 3041-keV transitions in prompt coincidence with the transitions feeding the isomer. They are included in Fig. 1(b) and Table I for completeness. Similarly, the 33 keV $1/2^- \rightarrow 3/2^-$ transition cannot be observed in the present experiment because of our low-energy threshold of some 60 keV, and the spectroscopy of the 741-keV $3/2^- \rightarrow 7/2^-$ ground-state transition is hampered by the relatively long-half-life of the $3/2^-$ state ($T_{1/2} = 63.5(14)$ ns [3]).

Figure 2 provides a prompt γ -ray spectrum from the two Gammasphere experiments, which is in coincidence with one α particle, two protons, and one neutron detected in Microball and the Neutron Shell, respectively. The contaminations from the above-mentioned reaction channels were carefully subtracted (i.e., the spectrum provides a necessary and sufficient condition for transitions belonging to ^{53}Fe). The spectrum served also as the basis for the relative intensities in Table I. Next to the well-known 287-, 836-, 1011-, 1328-, and 2339-keV transitions, which connect the low-spin yrast states, intense transitions at 499, 963, 1771, 3325, and 3788 keV are visible. They form the skeleton of the high-spin part of the level scheme in Fig. 1(b). With a few exceptions, all transitions in Fig. 2 with relative intensities of about 1% of the intensity of the 1328-keV line could be placed in the present level scheme of ^{53}Fe .

The low-spin part of the decay scheme of ^{53}Fe in Fig. 1(a) is by and large in agreement with the most recent data evaluation [3]. The only difference is a change of the spin value of the 2843-keV state from $7/2^-$ in Ref. [3] to $11/2^-$ in the present decay scheme. The assignment is based on angular distributions and correlations of both populating and depopulating transitions of the 2843-keV state (cf. Table I). Figure 3(b) provides a γ -ray spectrum in the respective region of the level scheme. It is in coincidence with the 2445-keV doublet. The 2445-keV transition connecting the 4785- and 2339-keV levels sees both the 1011- and 1328-keV transitions in the yrast cascade and is responsible for the peaks at 1112 and 1287 keV in Fig. 3(b). The 2445-keV transition between

the 3774- and 1328-keV levels adds statistics to the 1328-keV ground-state transition in Fig. 3(b) and is responsible for the 781-, 1157-, and 1566-keV lines in the spectrum. The weak transition at 1492 keV could not be placed in the level scheme.

Figure 3(a) focuses on the low-spin portion of the level scheme on the left-hand side of Fig. 1(a). The spectrum is in coincidence with the new 1134-keV $9/2^- \rightarrow 5/2^-$ transition. The 648- and 683-keV lines, which depopulate the known 1424-keV state are clearly seen as well as the continuation of the sequence via the 755- and 1695-keV lines. The peaks at 411 and 1408 keV arise from the ^{54}Fe yrast cascade, namely via the 1130 keV $4^+ \rightarrow 2^+$ transition [19]. Figure 3(c) is in coincidence with the intense 287-keV $15/2^- \rightarrow 13/2^-$ transition. In addition to the transitions belonging to the yrast sequence, peaks are visible at 1092, 1876, 2434, 3175, 3226, 3472, 3676, and 3751 keV. With the exception of the 3175 keV line, which populates the 4005 keV $17/2^-$ state, all of them are found to feed the 3463 keV 15^- level and connect to nonyrast $15/2^-$, $17/2^-$, and $19/2^-$ states. For the sake of clarity, the transitions at 3226, 3676, and 3751 keV have not been included in Fig. 1.

Figure 3(e) provides a spectrum in coincidence with the high-energy 4362 keV γ ray, which has been placed in the new high-spin regime. The yrast transitions between the 7328 keV $25/2^-$ state and the $19/2^-$ isomer at 499, 963, 3325, and 3788 keV are clearly visible, as well as a peak at 903 keV, which thus is placed on top of the 11690-keV level. The angular distribution ratio of the 4362 keV line, $R_{150-97} = 0.54(11)$, is a clear indication for the dipole character of that transition.

The spectrum in Fig. 3(d) has been measured in coincidence with the 963-keV $25/2^- \rightarrow 21/2^-$ and 965-keV $17/2^- \rightarrow 19/2^-$ doublet, the existence of which is apparent through the appearance of the “self-coincident” peak at 964 keV. The most intense transitions at 1771 and 3325 keV as well as the line at 2094-keV mark the yrast sequence within this high-spin part of the level scheme. The angular distribution and correlation results of the 1771-keV line point at an almost pure dipole transition, whereas the values for the high-energy 3325-keV line require a considerable quadrupole admixture, $\delta(E2/M1) \sim -1$. Because of the relatively large uncertainties, the multipole character of the 2094-keV transition cannot

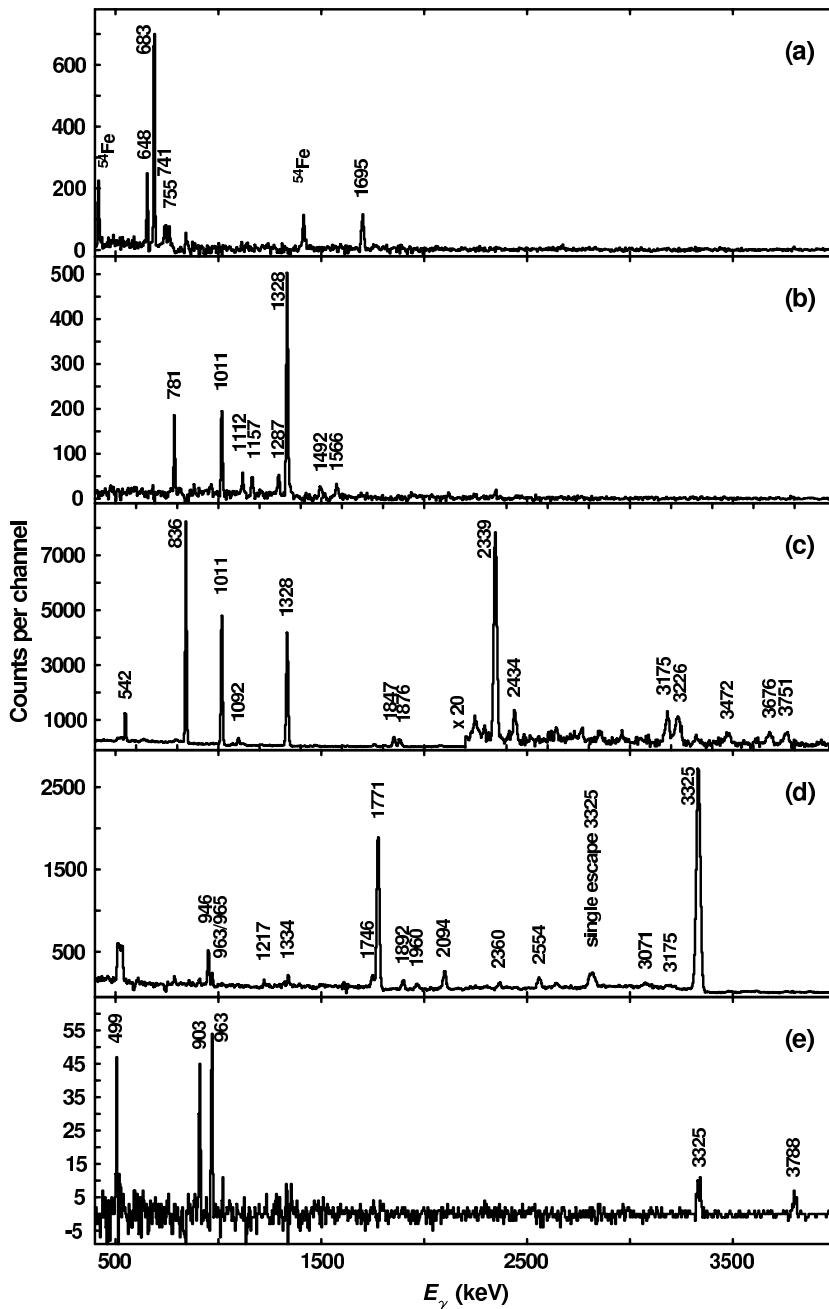


FIG. 3. γ -ray spectra in coincidence with one α particle, two protons, and one neutron from the two Gammasphere experiments. Panel (a) is in coincidence with the 1134-keV $9/2^- \rightarrow 5/2^-$ transition decaying from the 2558-keV level, panel (b) is in coincidence with the 2445-keV doublet decaying from the 3774- and 4785-keV levels, respectively, and panel (c) is in coincidence with the intense 287-keV $15/2^- \rightarrow 13/2^-$ yrast transition. These three spectra provide examples for the data quality of the low-spin part of the level scheme of ^{53}Fe shown in Fig. 1(a). Panels (d) and (e) are in coincidence with the 963-keV $25/2^- \rightarrow 21/2^-$ yrast transition and the high-energy 4362-keV $27/2^- \rightarrow 25/2^-$ transition, respectively. They illustrate the newly established high-spin part of the level scheme of ^{53}Fe displayed in Fig. 1(b). The energy labels next to the peaks are in kilo-electron-volts.

be fixed. However, its relative intensity hints toward an yrast transition, and the tentative existence of the 3865-keV transition provides further confidence in a $(29/2^-)$ assignment to the 11192-keV level. The 946-, 1217-, 1960-, and 2554-keV peaks in Fig. 3(d) connect to nonyrast structures. Several combinations of angular distribution and correlation values in conjunction with the plain existence of certain transitions allow for firm spin and parity assignments to the states at 8273, 8544, and 9880 keV and tentative assignments to the levels at 7181, 9287, 9550, and 10876 keV.

The lines at 1334, 1746, 1892, 2360, and 3175 keV in Fig. 3(d) relate to the 965-keV $17/2^- \rightarrow 19/2^-$ transition. Whereas the former three belong to the low-spin region of the ^{53}Fe level scheme, the latter two form important connections

between the two parts of the level scheme, namely between the yrast and (tentative) yrare $21/2^-$ states toward the 4005-keV yrast $17/2^-$ state. Though associated with large uncertainties, the angular distribution ratios of the 2360- and 3175-keV transitions are consistent with stretched $E2$ character.

Finally, in the thin target experiments, the 1445-, 1606-, 1771-, and 2094-keV transitions reveal significant additional Doppler shifts with respect to the applied generic event-by-event Doppler correction. This correction is based on recoils, which are supposed to have left the thin target foil before the γ -ray emission occurred, and thus includes a slowing down process inside the target foil. If, however, the γ -rays were emitted while the recoils are slowing down inside the thin target foil, they would be emitted with on average higher velocities

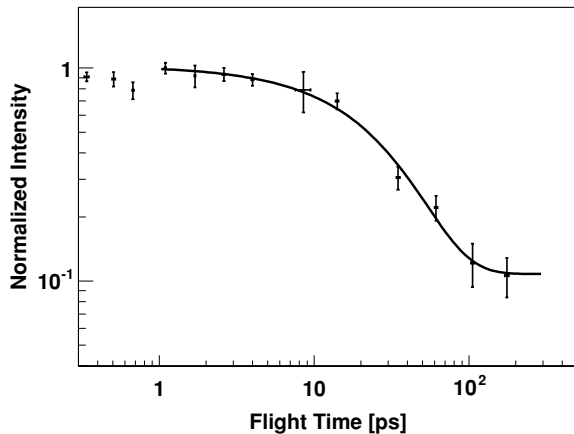


FIG. 4. Decay curve of the unshifted component of the 963-keV transition in ^{53}Fe for 13 effective flight distances measured in coincidence with the shifted component of the 1771-keV transition.

(i.e., yield additional Doppler shifts). Therefore, the time it takes for the recoils to pass through the thin target foil, $t_{\text{pass}} \sim 0.2$ ps, represents an upper limit for the effective lifetimes of the states at 8273, 9098, 9880, and 11192 keV.

The lifetimes of the 6365- and 7328-keV states are determined from the GASP experiment using the RDDS technique as described in the previous section. Figure 4 illustrates the decay curve of the unshifted portion of the 963-keV $25/2^- \rightarrow 21/2^-$ transition in ^{53}Fe . The data points were least-squares fitted to an exponential with a constant background. The result is $\tau = 26.2(32)$ ps for the 7328-keV $25/2^-$ state. To avoid any influence from the short-lived 9098-keV state ($\tau < 0.2$ ps), the starting point for the fits was set to 1 ps. This is five times the estimated upper limit of the 9098-keV level, and the 1771-keV line should effectively have no longer stopped components (i.e., full statistics are seen in the coincidence spectra used in the analysis).

Because the intensity of the unshifted part of the 3325-keV $21/2^- \rightarrow 19/2^-$ transition is measured in coincidence with the shifted part of the 1771-keV transition, its decay curve represents an effective lifetime of the $25/2^-$ and $21/2^-$ states. Therefore, the decay curve of the 3325-keV line was least-squares fitted with two lifetime components, which allows estimation of an upper limit for the lifetime of the 6365-keV $21/2^-$ state. One of the lifetime components used in the fit was fixed to a value corresponding to the lower limit of the lifetime of the $25/2^-$ state. As for the analysis of the 963-keV transition, the starting point for the fit was set to 1 ps. The result indicates $\tau < 4$ ps for the 6365-keV $21/2^-$ state.

V. SHELL-MODEL INTERPRETATION

To interpret the excited negative-parity states in ^{53}Fe large-scale shell-model calculations were performed using the shell-model code ANTOINE [21,22]. The calculations employ the full fp space comprising the $1f_{7/2}$ orbit below and the $2p_{3/2}$, $1f_{5/2}$, and $2p_{1/2}$ orbits above the $N, Z = 28$ shell closure. The configuration space was truncated to allow for five particle excitations from the $1f_{7/2}$ shell into the

TABLE II. Mean-level deviations, binding-energy shifts, and mean branching deviations of the yrast sequence in ^{53}Fe for the four different shell-model calculations performed.

Interaction	MLD [keV]	BES [keV]	MBD
kb3g	268	-146	0.15
kb3g_coul	249	-64	0.14
gxfp1	193	71	0.18
gxfp1_coul	206	144	0.18

upper fp shell. Calculations performed on the $1f_{7/2}$ yrast structure in $A = 50$, $A = 51$, and $A = 52$ nuclei using this configuration space have been shown to give results more or less indistinguishable from calculations performed in the full fp configuration space [1]. Two interactions have been studied: The standard KB3G [1] and GXPF1 [23] interactions without any Coulomb interaction (kb3g, gxfp1) and with theoretical harmonic-oscillator Coulomb matrix elements (kb3g_coul, gxfp1_coul). The calculations are done with bare g factors and effective nucleon charges taken from Ref. [6] (i.e., $\varepsilon_p = 1.16e$ and $\varepsilon_n = 0.78e$ for protons and neutrons, respectively). The experimental γ -ray energies were used to compute transition strengths and deduce branching ratios and mixing ratios of the transitions and lifetimes of the nuclear states.

In Fig. 5 the calculated energy values are compared with the observed excitation energies for the yrast structure starting at spin $I^\pi = 7/2^-$ and up to spin $29/2^-$. The agreement for these states is overall very good, which is manifested by the rather small values of mean-level deviations (MLD) and binding-energy shifts (BES) presented in Table II.

The BES is chosen to minimize the MLD and enables a quantitative comparison of states at different excitation energies. Although there is no major difference between the calculations with and without the Coulomb interaction, there are two discrepancies between the different interactions. KB3G predicts a too-large gap just above the $19/2^-$ level, which is almost perfectly reproduced with GXFP1. Conversely, GXFP1 seems to have some problems with the distance between the $27/2^-$ and $29/2^-$ states, for which KB3G yields preferred numbers. Because the latter minor disagreement affects only two states, whereas the former acts on three levels, the MLD values for GXFP1 turn out to be somewhat smaller than those for KB3G.

To better estimate the quality of the predicted wave functions one should compare the electromagnetic properties rather than the excitation energies. Therefore, the experimental and calculated branching ratios for the yrast cascade are compared and the corresponding mean branching deviations (MBD) [24,25] are calculated. They are also included in Table II. As for the level energies, the branching ratios are overall very well reproduced. One problem common to all parametrizations is the decay of the yrast $17/2^-$ state. Experimentally an almost 50:50 distribution toward the $15/2^-$ and $19/2^-$ levels is observed, whereas the calculations predict an almost exclusive branch into the $19/2^-$ isomer, probably based on an $M1$ spin-flip transition within the seniority $\nu = 3$ scheme. In reality, however, the $17/2^-$ state may comprise more core-excited components. Although this problem is the only one for KB3G, GXFP1 also fails to

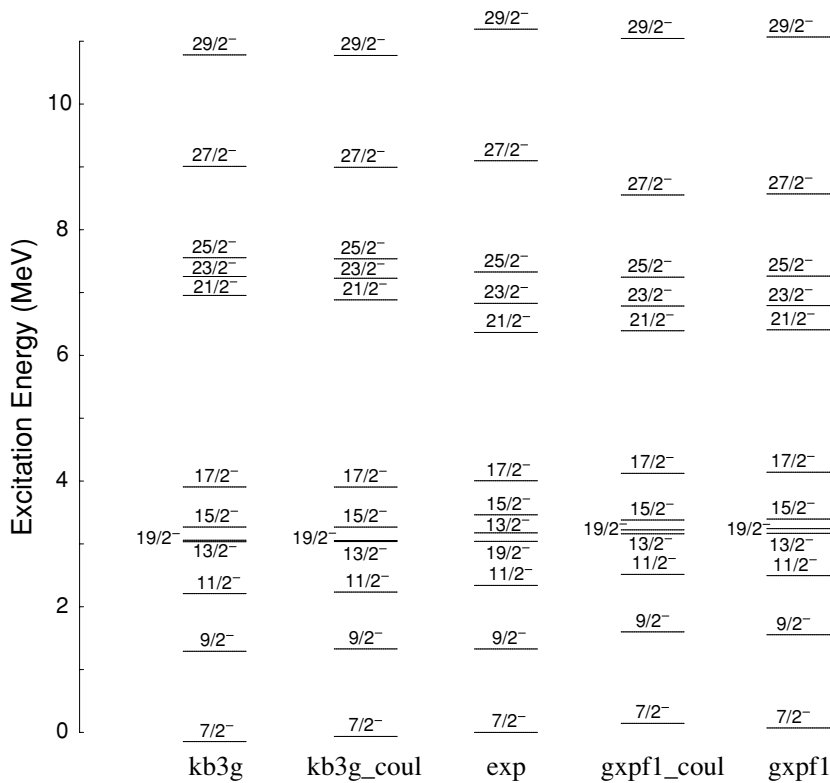


FIG. 5. Experimental and calculated excitation energies for the observed yrast sequence between $I^\pi = 7/2^-$ and $I^\pi = 29/2^-$ states. For all calculated states the binding energy shift (cf. Table II) has been added to the excitation energies.

describe the experimentally well-established branching ratios of the 499- and 963-keV transitions depopulating the $25/2^-$ state. Here, GXFP1 favors the 499-keV branch approximately 60:40, whereas the experiment demands 25:75. This additional disagreement explains the somewhat higher MBD value of the GXFP1 calculations in Table II.

Even for the yrare states, the agreement between experimental and calculated branching ratios is pretty good, although being somewhat worse than for the yrast sequence. This implies that the previously unknown states in ^{53}Fe are generally well described in the present shell-model calculations. This is also true for the predictions of lifetimes: KB3G and GXFP1 yield 25 and 17 ps for the lifetime of the 7328-keV state, respectively. Either interaction predicts lifetimes shorter than 0.1 ps for the 6365-, 8273-, 9098-, 9880-, and 11192-keV states, which is consistent with the data (cf. Table I).

VI. SUMMARY AND CONCLUSIONS

A new extensive level scheme of the even-odd nucleus ^{53}Fe is presented. The lifetime of the yrast $25/2^-$ state and an

upper limit for the lifetime of the yrast $21/2^-$ state has been determined via the RDDS method. A thorough and detailed comparison of excitation energies and electromagnetic decay properties with large-scale shell-model calculations in the fp shell has been performed. Two different interactions have been studied using effective charges taken from Ref. [6] and bare g factors. The comparison indicates an overall very good agreement, even though some distinct local disagreements remain.

ACKNOWLEDGMENTS

We thank the accelerator crews and the Gammasphere and GASP support staff at Argonne, Berkeley, and Legnaro for their supreme efforts. This work is supported in part by the Swedish Research Council, the European Commission under contract number HPRI-1999-CT-00083, the European Community programme IHP under contract number HPMF-CT-2002-02018, and the U.S. Department of Energy under grants DE-AC03-76SF00098 (LBNL), DE-FG05-88ER-40406 (WU), and W-31-109-ENG38 (ANL).

- [1] A. Poves *et al.*, Nucl. Phys. **A694**, 157 (2001).
- [2] S. J. Williams *et al.*, Phys. Rev. C **68**, 011301(R) (2003).
- [3] J. Huo, Nucl. Data Sheets **87**, 507 (1999).
- [4] S. J. Williams, Ph.D. thesis, Keele University, unpublished.
- [5] L. Frankland, Ph.D. thesis, University of Brighton, 2001.
- [6] R. du Rietz *et al.*, Phys. Rev. Lett. **93**, 222501 (2004).
- [7] I.-Y. Lee, Nucl. Phys. **A520**, 641c (1990).

- [8] M. Devlin *et al.*, Nucl. Instrum. Methods Phys. Res. Sec. A **383**, 506 (1996).
- [9] D. G. Sarantites *et al.*, Nucl. Instrum. Methods Phys. Res. Sec. A **381**, 418 (1996).
- [10] D. G. Sarantites *et al.*, Nucl. Instrum. Methods Phys. Res. Sec. A **530**, 473 (2004).
- [11] A. Dewald *et al.*, Nucl. Phys. **A545**, 822 (1992).

- [12] C. Rossi-Alvarez, Nucl. Phys. News **3**, 3 (1993).
- [13] J. Ekman, D. Rudolph, C. Andreoiu, C. Fahlander, M. N. Mineva, M. A. Bentley, S. J. Williams, R. Charity, E. Ideguchi, W. Reviol, D. G. Sarantites, V. Tomov, R. M. Clark, M. Cromaz, P. Fallon, A. O. Macchiavelli, M. P. Carpenter, and D. Seweryniak, Phys. Rev. C **70**, 014306 (2004).
- [14] C. Andreoiu, Ph.D. thesis, Lund University (2002), ISBN 91-628-5308-2.
- [15] J. Ekman, Ph.D. thesis, Lund University (2004), ISBN-91628-6061-5.
- [16] D. C. Radford, Nucl. Instrum. Methods Phys. Res. Sec. A **386**, 297 (1995).
- [17] J. Theuerkauf, S. Esser, S. Krink, M. Luig, N. Nicolay, O. Stuch, and H. Wolters, program TV, University of Cologne, unpublished.
- [18] C. E. Svensson *et al.*, Nucl. Instrum. Methods Phys. Res. Sec. A **396**, 228 (1997).
- [19] D. Rudolph *et al.*, Eur. Phys. J. A **4**, 115 (1999).
- [20] H. J. Rose and D. M. Brink, Rev. Mod. Phys. **39**, 306 (1967).
- [21] E. Caurier, shell model code ANTOINE, IRES, Strasbourg 1989–2002.
- [22] E. Caurier and F. Nowacki, Acta Phys. Pol. **30**, 705 (1999).
- [23] M. Honma, T. Otsuka, B. A. Brown, and T. Mizusaki, Phys. Rev. C **65**, 061301(R) (2002).
- [24] D. Rudolph, K. P. Lieb, and H. Grawe, Nucl. Phys. **A597**, 298 (1996).
- [25] R. du Rietz, Ph.D. thesis, Lund University (2005), ISBN-91-628-6394-0.